Gigabar Spherical Shock Generation on the OMEGA Laser

R. Nora,[1,2,3] W. Theobald,[1] R. Betti,[1,2,3] F. J. Marshall,[1] D. T. Michel,[1] W. Seka,[1] B. Yaakobi,[1] M. Lafon,[1] C. Stoeckl,[1] J. Delettrez,[1] A. A. Solodov,[1] A. Casner,[4] C. Reverdin,[4] X. Ribeyre,[5] A. Vallet,[5] J. Peebles,[6] F. N. Beg,[6,2] and M. S. Wei[7,2]

[1]*Laboratory for Laser Energetics, University of Rochester, 250 East River Road, Rochester, New York 14623, USA*
[2]*Fusion Science Center, University of Rochester, Rochester, New York 14623, USA*
[3]*Department of Physics and Astronomy and/or Mechanical Engineering, University of Rochester, Rochester, New York 14623, USA*
[4]*CEA, DAM, DIF, F-91297 Arpajon, France*
[5]*Université de Bordeaux-CNRS-CEA, CELIA (Centre Lasers Intenses et Applications) UMR 5107 F-33400 Talence, France*
[6]*University of California, La Jolla, California 92093, USA*
[7]*General Atomics, San Diego, California 92121, USA*
(Received 25 July 2014; published 27 January 2015)

This Letter presents the first experimental demonstration of the capability to launch shocks of several-hundred Mbar in spherical targets—a milestone for shock ignition [R. Betti *et al.*, Phys. Rev. Lett. 98, 155001 (2007)]. Using the temporal delay between the launching of the strong shock at the outer surface of the spherical target and the time when the shock converges at the center, the shock-launching pressure can be inferred using radiation-hydrodynamic simulations. Peak ablation pressures exceeding 300 Mbar are inferred at absorbed laser intensities of $\sim 3 \times 10^{15}$ W/cm^2. The shock strength is shown to be significantly enhanced by the coupling of suprathermal electrons with a total converted energy of up to 8% of the incident laser energy. At the end of the laser pulse, the shock pressure is estimated to exceed ~1 Gbar because of convergence effects.

DOI: 10.1103/PhysRevLett.114.045001 PACS numbers: 52.57.-z, 52.38.-r

It was recently shown [1–7] that the gain of an inertial confinement fusion implosion can be significantly enhanced by launching a strong spherically convergent shock at the end of the compression (or assembly) pulse. This two-step scheme is usually referred to as shock ignition (SI). Shock ignition has a distinct advantage over fast ignition [8] because it reduces the energy required for ignition as compared to that of conventional hot-spot ignition [9] while still using a single laser. Recent two-dimensional simulations [3,10] have indicated the possibility of achieving ignition at submegajoule laser energies. While implosion experiments on the OMEGA laser [11], using 60-beam symmetric implosions of CH shells filled with D_2, have demonstrated a 4× increase in yield and a 40% increase in shell areal density for SI pulse shapes when compared to conventional implosions [12], the final shock strength was much lower than the value required for ignition.

Demonstrating the capability to generate shocks of the order of $\gtrsim$300 Mbar at laser intensities in the range of 10^{15} to 10^{16} is crucial to the long-term success of SI. This Letter reports on the first shock and ablation pressures inferred in spherical geometry using an x-ray flash as the primary diagnostic. Investigations determining the shock strength in planar geometries have been completed at LULI [13], OMEGA [14], and PALS [15], where the greatest shock pressure reported is ~90 Mbar at intensities $\leq 10^{16}$ W/cm^2. The spherical platform can be extended to carry out fundamental high-energy-density physics experiments to explore material properties at gigabar pressures [16] or scrutinize suprathermal electron preheat [17] and shock timing [18].

The targets were composed of 430-to 600-μm outer-diameter solid spheres of 5% titanium-doped plastic in which the outer 50 μm consisted of pure CH (see Fig. 1). They were illuminated by a 2-ns laser pulse with a 1-ns, low-intensity foot used to create a coronal plasma followed by a 1-ns, high-intensity square pulse with 22–27 kJ of laser energy. Small spot phase plates [19] were used to increase

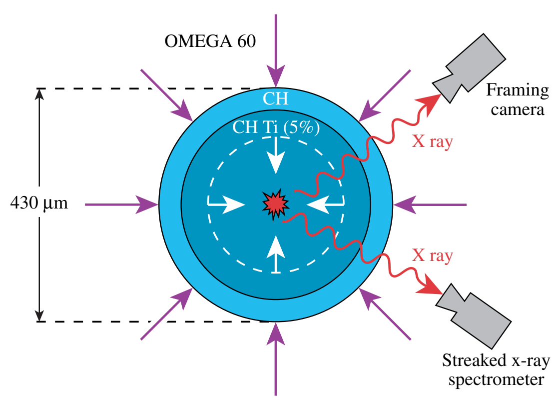

FIG. 1 (color online). Experimental setup used to infer the shock and laser ablation pressure at SI-relevant intensities.

the on-target incident intensity up to $\sim 6 \times 10^{15}$ W/cm^2 at the initial target surface, both with and without smoothing by spectral dispersion (SSD) [20]. The rapid rise in laser intensity by the high-intensity square pulse generated an inwardly propagating shock wave that converged at the center of the target, raising the temperature in a very small volume to hundreds of eV and resulting in the self-emission of x-rays in the keV range. The seed shock pressure is inferred from hydrodynamic simulations constrained by the measured temporal occurrence of the x-ray flash.

The x-ray emission from the center of the target was measured temporally and spatially and spectrally resolved using an x-ray framing camera (XRFC) [21] and a streaked x-ray spectrometer (SXS) [22]. The XRFC spatially and temporally resolved the x-ray emission, using a 4×4 pinhole array to produce 16 enlarged images of the target on a microchannel-plate detector, which was covered with four strips of gold film. A 200-μm Be foil and a thin (12-μm) Ti foil placed in front of the detector, combined with the spectral response of the diagnostic, restricted the range of recorded x-rays to $\sim$3 to 7 keV. Figure 2 shows a portion of the raw data collected with the XRFC for a typical experiment. At early times, the observed emission comes from the hot corona when the laser is still interacting with the target, and as time progresses, the laser shuts off and the corona cools. After a brief period of time, the appearance of a small but bright source of x-rays originating from the center of the target is observed. The x-ray emission was measured from a very small region with a diameter of less than $\sim$15 μm (full width at half maximum). The simultaneously operated SXS captured this line emission and determined the temporal width of the emitted intensity to be shorter than $\sim$50 ps. The temporal occurrence of the x-ray flash between the two detectors is within the absolute timing error of each other.

Copious amounts of suprathermal electrons are generated when the thresholds for two-plasmon-decay (TPD) and stimulated Raman scattering (SRS) instabilities are exceeded during the high-intensity square pulse [23]. The temperature of the suprathermal electrons and the temporal dependence were measured with a time-resolved, four-channel hard x-ray detector (HXRD) [24] and two time-integrated imaging-plate diagnostics HERIE [25] and BMXS [26]. Typical temperatures measured for the suprathermal electrons can be fit to single-temperature Maxwellian distributions with central temperatures in the range of 50—100 keV. Up to 2 kJ ($\sim$8% of the total incident laser energy and 15% instantaneously) of suprathermal electrons were inferred to be deposited into the target by comparing the measured bremsstrahlung emission to Monte Carlo simulations, assuming that the suprathermal electrons were generated isotropically. Figure 3 shows that the measured total energy of the suprathermal electrons increases with the total laser energy and is dependent on whether or not the SSD is functioning. The integrated intensity of the x-ray emission from shock convergence was measured with a gated microscope x-ray imager [27]. Figure 4 shows the analysis of two experiments with similar incident laser energies. A $\sim 25\times$ increase in the shock-flash x-ray intensity was observed when SSD was not operating (2.2 kJ of suprathermal electrons and 27 kJ of laser energy) with respect to the case of SSD on (0.8 kJ of suprathermal electrons and 24 kJ of laser energy). The large increase in x-ray intensity and an earlier x-ray flash time indicates that the strength of the shock was greatly enhanced most likely by the suprathermal electrons. Measured time-resolved spectra for Raman, $\omega/2$, and $3\omega/2$ emissions show that both TPD and SRS are active. The observation of moderate suprathermal electron temperatures at these laser intensities has a significant impact on SI designs since they can enhance the ignitor shock [28] and improve the implosion performance [10,28].

The shock and ablation pressures are inferred by constraining radiation-hydrodynamic simulations to the

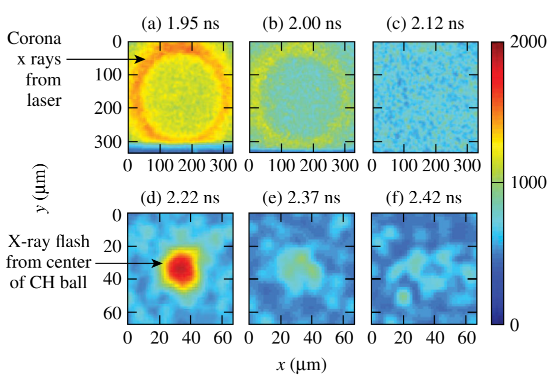

FIG. 2 (color online). An x-ray framing camera captured a short x-ray flash at the time when the shock converged in the center. The timing in each frame gives the peak time of the electrical gating pulse relative to the start of the laser pulse. The color bar indicates the measured emission intensity in arbitrary units.

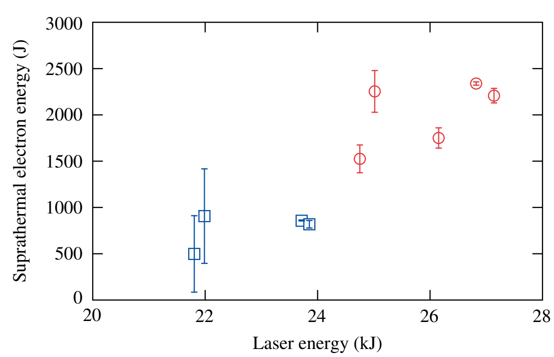

FIG. 3 (color online). Total energy converted into suprathermal electrons versus laser energy. Blue squares indicate that SSD was on, whereas red circles indicate that SSD was off. Up to $\sim$8% of the total laser energy was converted into suprathermal electrons at moderate temperatures (50–100 keV). The error bars represent half the difference between HERIE and BMXS.

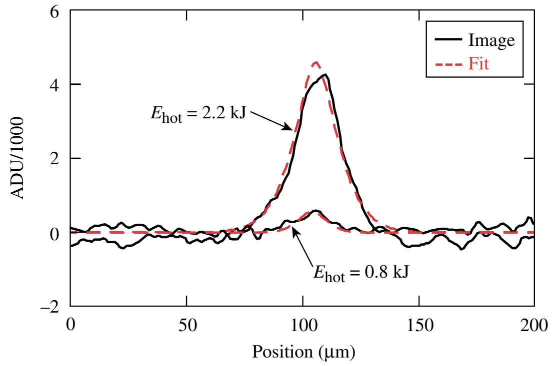

FIG. 4 (color online). Integrated x-ray (2–6 keV) intensity lineouts from the center of the target for two shots with 27 kJ of laser energy and 2.2 kJ of suprathermal electron energy (upper curves) and 24 kJ of laser energy and 0.8 kJ of suprathermal electron energy(lower curves).

experimental observables: the temporal occurrence of the x-ray emission, the suprathermal electron energy and temperature distribution, and the temporal evolution of the hard x-ray emission (see Fig. 5). The simulations used the radiation-hydrodynamic code LILAC [29] and were run with a multigroup radiation diffusion model, Thomas-Fermi [30] or SESAME [31,32] equations of state (EOS), flux-limited thermal transport [33], and a suprathermal electron-transport package [34]. The suprathermal electron-transport package is a straight-line deposition model whereby a fraction of the laser energy reaching the quarter-critical surface is converted into suprathermal electrons with a single-temperature Maxwellian distribution and 2π forward divergence. The stopping range of the suprathermal electrons is modeled via collisional effects and is computed based on the work by Solodov and Betti [35]. The flux limiter, which is the only free parameter within the radiation-hydrodynamic simulations, is adjusted to match the experimentally measured x-ray flash time. Each simulation is, in principle, constrained by its own x-ray flash time and therefore has a unique flux limiter ranging from 5% to 8%; however, choosing 6.5% constrains all of the simulations within the experimental error bars. The ablation pressure is the pressure in the shell at the position where the material velocity is zero in the lab frame, an accurate approximation for slowly imploding solid spheres.

Figure 6 illustrates the shock and ablation pressure inferred from a typical simulation that matches all of the experimental observables. The ablation pressure (blue curves) increases as a function of time, due to both thermal conduction of the absorbed laser energy and the energy deposition by suprathermal electrons, and decays soon after the laser is shut off. Meanwhile, the shock pressure (red curves) rapidly increases in time due to convergence effects [36]. For the particular shot shown in Fig. 6, the shock pressure is inferred to exceed 1 Gbar when the shock is $\sim$25 μm from the center of the target. Additionally, simulations including suprathermal electrons (solid curves in Fig. 6) are observed to significantly enhance the shock and ablation pressures by up to $\sim$50% instantaneously over the case when the simulation is repeated in the absence of suprathermal electrons (dotted curves in Fig. 6). This result is corroborated with recent theoretical work showing $\sim$300-Mbar shock pressures can be generated solely due to suprathermal electrons [37–39].

Inspection of Fig. 6 illustrates that a significant fraction of the energy carried by suprathermal electrons is deposited beyond the ablation front and contributes to the overall shock strength. In this specific example at 1.6 ns, only suprathermal electrons with temperatures less than 60 keV

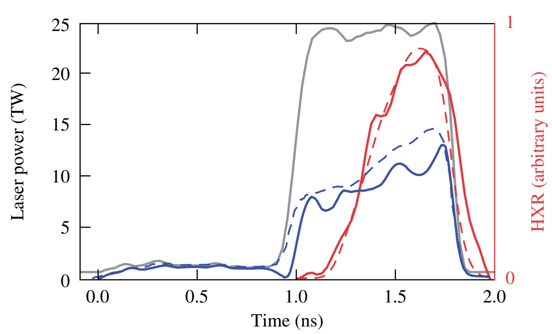

FIG. 5 (color online). Comparison of experimental (solid lines) and simulated (dashed lines) curves for shot 71589 with incident laser power (gray line), laser absorption (blue lines), and hard x-ray emission (red lines) resulting from suprathermal electrons (in arbitrary units). The experimental hard x-ray emission was averaged over the three highest HXRD channels and has a $\pm$5% uncertainty due to noise and deconvolution error. The absorption data are averaged over two scattered light diagnostics each with an uncertainty of $\pm$5%.

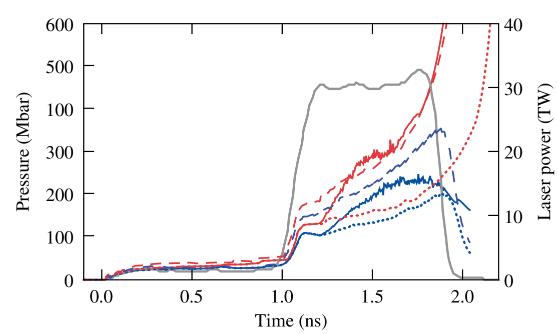

FIG. 6 (color online). Simulated ablation pressure (blue lines) and shock pressure (red lines) as a function of time for shot 72679. The solid lines indicate a simulation that matches all experimentally observed quantities using a flux limiter of 5%. The dotted lines are the simulation results in the absence of suprathermal electrons (flux limiter of 5%). The dashed lines indicate a simulation that also matches the x-ray flash time but in the absence of suprathermal electrons (the flux limiter was increased to 8%). For reference, the solid gray line indicates the laser pulse.

are stopped before the ablation surface, corresponding to ∼12% of the total energy in a 70 keV Maxwellian distribution, while suprathermal electrons with temperatures from 60 to 200 keV are stopped between the ablation and shock front, corresponding to ∼55% of the total suprathermal energy. Therefore, using the ablation pressure as a metric to describe the conversion of laser energy into a shock strength is no longer valid. A more-effective metric in this case would be to adjust the energy transport model to simulate the effect of suprathermal electrons on the shock strength and observe a new "effective ablation pressure." The effective ablation pressure (dashed curves in Fig. 6) drives the shock at the same velocity as when suprathermal electrons are included (solid curves in Fig. 6) but without the use of suprathermal electrons. This is achieved by increasing the flux limiter and is unique to each shot in the campaign. Physically, this can be explained by the fact that a shock must travel from the outside of the target to the center in the measured period of time regardless of how the energy is transferred. Therefore, whether the shock is solely driven by the rocket effect or by a combination of ablation pressure and suprathermal-electron energy deposition, the pressure behind the shock must be independent of the mechanism driving the shock and even insensitive of many physics details. Corroborating this point is the choice of EOS; whether using Thomas-Fermi or SESAME, the resulting shock pressure required to match the experimental observables remains the same despite differences in postshock mass density. The ambiguity in EOS could be solved by a direct measurement of the mass density (e.g., Ref. [16]).

The maximum ablation pressure $P_a^{\max}$ and effective maximum ablation pressure P_a^{eff} for all of the experiments are found to scale with the maximum absorbed laser power divided by the critical surface area $I_{15\text{abs}}$ in units of 10^{15} W/cm^2 via the following formulas:

$$P_a^{\max}(\text{Mbar}) \approx 90 I_{15\text{abs}}^{1.2}, \quad (1)$$

$$P_a^{\text{eff}}(\text{Mbar}) \approx 90 I_{15\text{abs}}^{1.4}, \quad (2)$$

and are shown in Fig. 7. The error bars in Fig. 7 are the result of adjusting the simulated x-ray flash time by ±50 ps as a result of the absolute error in the timing diagnostics, changing both the simulated absorbed laser intensity and ablation pressure. This scaling shows a significant departure from previous spherical ablation pressure scaling $P_a^{\text{theory}}(\text{Mbar}) \approx 100 I_{15\text{abs}}^{7/9}$ derived for low intensities ($\lesssim 10^{15}$ W/cm^2) due to collisional absorption [40]. The difference is likely due to the greater absorbed laser intensities as well as the presence of copious amounts of suprathermal electrons. Superimposing the ablation pressure scaling due to collisional absorption (Ref. [40]) with the pressure scaling due to suprathermal electrons from Refs. [37–39] with suitable parameters yields results

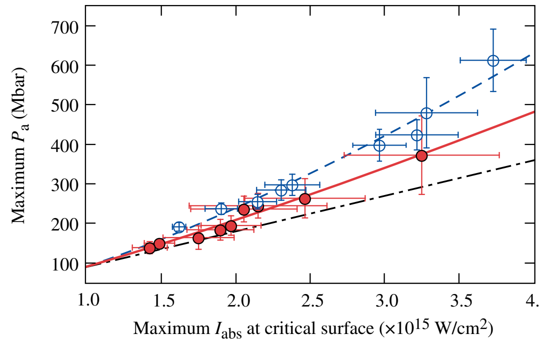

FIG. 7 (color online). Scaling of the inferred maximum ablation pressure with suprathermal electrons (solid red circles and solid line) and effective maximum ablation pressure without suprathermal electrons (open blue circles and dashed line) versus the maximum laser intensity that is absorbed at the critical surface for simulations matching all of the experimental observables. The black dash-dotted curve indicates the ablation pressure scaling for nonconstrained simulations without suprathermal electrons and a constant flux limiter value of 6.5%.

comparable to the inferred ablation pressures of this campaign; however, determining a physical formula to fully describe the complex behavior is beyond the scope of this Letter. Further analysis of simulations in the absence of suprathermal electrons shows that the exponent of the ablation pressure scaling varies with the choice of flux limiter; e.g., choosing the typical value of 6.5% yields a linear dependence on the absorbed laser intensity (black dash-dotted curve in Fig. 7). Comparing this curve with Eq. (1) demonstrates the enhancement suprathermal electrons have on the ablation pressure.

Extrapolating Eqs. (1) and (2) to the absorbed laser intensities of about $\sim 7 \times 10^{15}$ W/cm^2 used in the 700-kJ National Ignition Facility (NIF) [41] SI point design of Ref. [10], one finds ablation pressures that significantly exceed the required ∼600 Mbar (0.9 Gbar and 1.3 Gbar, respectively), indicating predicted ablation pressures to be high enough for robust ignition. However, NIF-scale ignition targets are much larger than those used in these OMEGA experiments, thereby leading to longer-scale-length plasmas at the time of shock launch. Higher levels of laser-plasma instabilities are expected, and a simple extrapolation of Eqs. (1) and (2) to NIF-scale plasmas may not be applicable. Therefore, despite these encouraging results obtained on OMEGA, an accurate extrapolation of the ablation pressure to NIF requires experiments on NIF-scale targets.

This material is based upon work supported by the Department of Energy National Nuclear Security Administration under Award No. DE-NA0001944, the Office of Fusion Energy Sciences No. DE-FG02-04ER54789, the University of Rochester, and the New York State Energy Research and Development Authority. The support of the U.S. DOE does not constitute an endorsement by that agency of the views expressed in this Letter.

[1] R. Betti, C. D. Zhou, K. S. Anderson, J. L. Perkins, W. Theobald, and A. A. Solodov, Phys. Rev. Lett. **98**, 155001 (2007).
[2] L. J. Perkins, R. Betti, K. N. LaFortune, and W. H. Williams, Phys. Rev. Lett. **103**, 045004 (2009).
[3] X. Ribeyre, G. Schurtz, M. Lafon, S. Galera, and S. Weber, Plasma Phys. Controlled Fusion **51**, 015013 (2009).
[4] M. Lafon, X. Ribeyre, and G. Schurtz, Phys. Plasmas **20**, 022708 (2013).
[5] A. J. Schmitt, J. W. Bates, S. P. Obenschain, S. T. Zalesak, and D. E. Fyfe, Phys. Plasmas **17**, 042701 (2010).
[6] S. Atzeni, X. Ribeyre, G. Schurtz, A. Schmitt, B. Canaud, R. Betti, and L. Perkins, Nucl. Fusion **54**, 054008 (2014).
[7] D. Batani, S. Baton, A. Casner, S. Depierreux, M. Hohenberger, O. Klimo, M. Koenig, C. Labaune, X. Ribeyre, C. Rousseaux *et al.*, Nucl. Fusion **54**, 054009 (2014).
[8] M. Tabak, J. Hammer, M. E. Glinsky, W. L. Kruer, S. C. Wilks, J. Woodworth, E. M. Campbell, M. D. Perry, and R. J. Mason, Phys. Plasmas **1**, 1626 (1994).
[9] J. Nuckolls, L. Wood, A. Thiessen, and G. Zimmerman, Nature (London) **239**, 139 (1972).
[10] K. S. Anderson, R. Betti, P. W. McKenty, T. J. B. Collins, M. Hohenberger, W. Theobald, R. S. Craxton, J. A. Delettrez, M. Lafon, J. A. Marozas *et al.*, Phys. Plasmas **20**, 056312 (2013).
[11] T. Boehly, D. Brown, R. Craxton, R. Keck, J. Knauer, J. Kelly, T. Kessler, S. Kumpan, S. Loucks, S. Letzring *et al.*, Opt. Commun. **133**, 495 (1997).
[12] W. Theobald, R. Betti, C. Stoeckl, K. S. Anderson, J. A. Delettrez, V. Y. Glebov, V. N. Goncharov, F. J. Marshall, D. N. Maywar, R. L. McCrory *et al.*, Phys. Plasmas **15**, 056306 (2008).
[13] S. D. Baton, M. Koenig, E. Brambrink, H. P. Schlenvoigt, C. Rousseaux, G. Debras, S. Laffite, P. Loiseau, F. Philippe, X. Ribeyre *et al.*, Phys. Rev. Lett. **108**, 195002 (2012).
[14] M. Hohenberger, W. Theobald, S. X. Hu, K. S. Anderson, R. Betti, T. R. Boehly, A. Casner, D. E. Fratanduono, M. Lafon, D. D. Meyerhofer *et al.*, Phys. Plasmas **21**, 022702 (2014).
[15] D. Batani, L. Antonelli, S. Atzeni, J. Badziak, F. Baffigi, T. Chodukowski, F. Consoli, G. Cristoforetti, R. De Angelis, R. Dudzak *et al.*, Phys. Plasmas **21**, 032710 (2014).
[16] A. Kritcher, T. Döppner, D. Swift, J. Hawreliak, G. Collins, J. Nilsen, B. Bachmann, E. Dewald, D. Strozzi, S. Felker *et al.*, High Energy Density Phys. **10**, 27 (2014).
[17] V. Smalyuk, D. Shvarts, R. Betti, J. A. Delettrez, D. H. Edgell, V. Y. Glebov, V. N. Goncharov, R. L. McCrory, D. D. Meyerhofer, P. B. Radha *et al.*, Phys. Rev. Lett. **100**, 185005 (2008).
[18] H. F. Robey, P. M. Celliers, J. D. Moody, J. Sater, T. Parham, B. Kozioziemski, R. Dylla-Spears, J. S. Ross, S. LePape, J. E. Ralph *et al.*, Phys. Plasmas **21**, 022703 (2014).
[19] S. P. Regan, T. C. Sangster, D. D. Meyerhofer, W. Seka, R. Epstein, S. J. Loucks, R. L. McCrory, C. Stoeckl, V. Y. Glebov, O. S. Jones *et al.*, J. Phys. Conf. Ser. **112**, 022077 (2008).
[20] S. Skupsky, R. W. Short, T. Kessler, R. S. Craxton, S. Letzring, and J. M. Soures, J. Appl. Phys. **66**, 3456 (1989).
[21] D. K. Bradley, P. M. Bell, J. D. Kilkenny, R. Hanks, O. Landen, P. A. Jaanimagi, P. W. McKenty, and C. P. Verdon, Rev. Sci. Instrum. **63**, 4813 (1992).
[22] M. Millecchia, S. P. Regan, R. E. Bahr, M. Romanofsky, and C. Sorce, Rev. Sci. Instrum. **83**, 10E107 (2012).
[23] J. F. Myatt, J. Zhang, R. W. Short, A. V. Maximov, W. Seka, D. H. Froula, D. H. Edgell, D. T. Michel, I. V. Igumenshchev, D. E. Hinkel *et al.*, Phys. Plasmas **21**, 055501 (2014).
[24] C. Stoeckl, V. Y. Glebov, D. D. Meyerhofer, W. Seka, B. Yaakobi, R. P. J. Town, and J. D. Zuegel, Rev. Sci. Instrum. **72**, 1197 (2001).
[25] R. Tommasini, J. A. Koch, B. Young, E. Ng, T. Phillips, and L. Dauffy, Rev. Sci. Instrum. **77**, 10E301 (2006).
[26] C. D. Chen, J. A. King, M. H. Key, K. U. Akli, F. N. Beg, H. Chen, R. R. Freeman, A. Link, A. J. Mackinnon, A. G. MacPhee *et al.*, Rev. Sci. Instrum. **79**, 10E305 (2008).
[27] F. J. Marshall and J. A. Oertel, Rev. Sci. Instrum. **68**, 735 (1997).
[28] R. Betti, W. Theobald, C. D. Zhou, K. S. Anderson, P. W. McKenty, S. Skupsky, D. Shvarts, V. N. Goncharov, J. A. Delettrez, P. B. Radha *et al.*, J. Phys. Conf. Ser. **112**, 022024 (2008).
[29] E. B. Goldman, LLE Report No. 16, Laboratory for Laser Energetics, University of Rochester, Rochester, NY, 1973.
[30] A. R. Bell, New Equations of State for Medusa, Rutherford and Appleton Laboratories, Chilton, Didcot, UK, 1980.
[31] G. I. Kerley, Phys. Earth Planet. Inter. **6**, 78 (1972).
[32] G. I. Kerley, Report No. SAND2003-3613, Sandia National Laboratory, Albuquerque, NM, 2003.
[33] R. C. Malone, R. L. McCrory, and R. L. Morse, Phys. Rev. Lett. **34**, 721 (1975).
[34] J. Delettrez and E. B. Goldman, LLE Report No. 36, Laboratory for Laser Energetics, University of Rochester, Rochester, NY, 1976.
[35] A. A. Solodov and R. Betti, Phys. Plasmas **15**, 042707 (2008).
[36] V. G. Guderley, Luftfahrtforschung **19**, 302 (1942).
[37] S. Gus'kov, X. Ribeyre, M. Touati, J.-L. Feugeas, P. Nicolai, and V. Tikhonchuk, Phys. Rev. Lett. **109**, 255004 (2012).
[38] X. Ribeyre, S. Gus'kov, J.-L. Feugeas, P. Nicolai, and V. T. Tikhonchuk, Phys. Plasmas **20**, 062705 (2013).
[39] A. R. Piriz, S. A. Piriz, and N. A. Tahir, Phys. Plasmas **20**, 112704 (2013).
[40] S. Atzeni, Plasma Phys. Controlled Fusion **42**, B143 (2000).
[41] G. H. Miller, E. I. Moses, and C. R. Wuest, Opt. Eng. (Bellingham, Wash.) **43**, 2841 (2004).